

## Kinetic study of wall collisions in a coaxial Hall discharge

Nathan B. Meezan and Mark A. Cappelli\*

*Department of Mechanical Engineering, Stanford University, Stanford, California 94305-3032*

(Received 29 March 2002; revised manuscript received 30 May 2002; published 11 September 2002)

Coaxial Hall discharges (also known as Hall thrusters, stationary plasma thrusters, and closed-drift accelerators) are cross-field plasma sources under development for space propulsion applications. The importance of the electron-wall interaction to the Hall discharge operation is studied through analysis of experimental data and simulation of the electron energy distribution function (EEDF) inside the discharge channel. Experimental time-average plasma property data from a laboratory Hall discharge are used to calculate the electron conductivity and to estimate the rate of wall-loss collisions. The electron Boltzmann equation is then solved in the local field limit, using the experimental results as inputs. The equation takes into account ionization and wall collisions, including secondary electrons produced at the wall. Local electron balances are used to calculate the sheath potential at the insulator walls. Results show an EEDF depleted at high energy due to electron loss to the walls. The calculated EEDFs agree well with experimental electron temperature data when the experimentally determined effective collision frequency is used for electron momentum transport. The electron wall-loss and wall-return frequencies are extremely low compared to those predicted by a Maxwellian of equal average energy. The very low frequency of wall collisions suggests that secondary electrons do not contribute to cross-field transport. This conclusion holds despite significant experimental uncertainty.

DOI: 10.1103/PhysRevE.66.036401

PACS number(s): 52.25.Fi, 52.25.Dg, 52.65.Ff, 52.40.Hf

### I. INTRODUCTION

Hall discharges are presently under development for use in space propulsion applications. In a Hall discharge (Fig. 1), the plasma is sustained in imposed orthogonal electric ( $\mathbf{E}$ ) and magnetic ( $\mathbf{B}$ ) fields. The discharge electrons, a large fraction of which are emitted by an external cathode, are magnetized, whereas the more massive propellant ions, usually xenon, are not. Consequently, the electrostatic fields established by the retarded electron flow accelerate the ions to high velocities, typically 50–80% of the discharge voltage. In a coaxial geometry, the electrons are constrained to move in the closed, azimuthal  $\mathbf{E} \times \mathbf{B}$  drift, with cross-field diffusion providing the necessary current to sustain the discharge. For this reason, the Hall discharge is a useful device for laboratory studies of electron transport in magnetized plasmas.

The efficiency of the Hall discharge as a rocket depends primarily on the current flowing through the discharge. One measurement of the thrust efficiency  $\eta$  of an electrostatic rocket is the ratio of the directed kinetic energy of the ions to the applied electrical power. The kinetic energy of the ions is determined by the applied voltage  $V$ , whereas the power is simply the product of the discharge voltage and current,

$$\eta = \frac{mv_i^2/2}{VI} = \frac{\xi VI_i}{VI} = \frac{\xi I_i}{I_i + I_e}.$$

Here,  $\xi$  is the efficiency of ion acceleration, and  $I_i$  and  $I_e$  are the ion and electron currents, respectively. Thus, for a given discharge voltage, the efficiency of the thruster is inversely proportional to the current. In some regions of the discharge (near the anode), the electrons carry most or all of the current, while in others (near the peak in the magnetic field), it

is desired that the electrons carry very little of the total current. A better understanding of the electron conductivity and what controls the flow of electrons throughout the discharge could allow the development of higher efficiency thrusters.

The electrons in Hall discharges exhibit anomalous cross-field transport: the conductivity is higher than that predicted by the simplest classical equations [1]. Electron transport in the Hall discharge is believed to be enhanced by fluctuations in the electric field and plasma density [2]. Collisions with the ceramic channel walls also play an important role in the discharge operation. In addition to impacting the kinetics of the Hall discharge plasma by shaping the electron energy distribution function (EEDF), the electron-wall interaction in

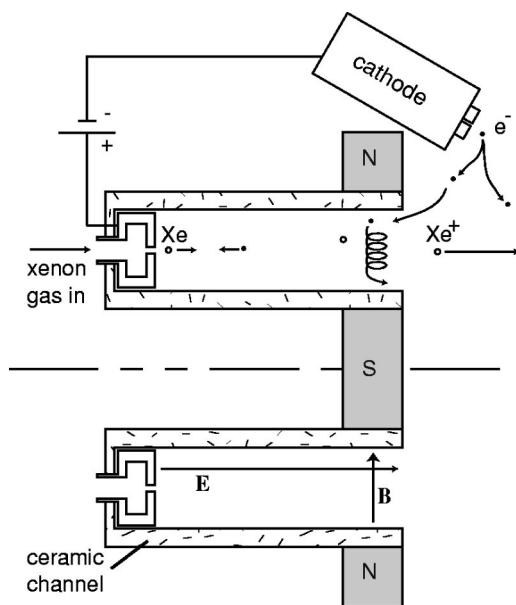


FIG. 1. Schematic of a typical coaxial Hall discharge accelerator.

\*Electronic address: cap@stanford.edu

the channel may also contribute to electron transport [3–5].

Several researchers have had moderate success in modeling the plasma inside the Hall discharge (and similar discharges) with hybrid fluid-particle codes [6–10] and full particle codes [11]. With the hybrid fluid-particle in cell codes, some investigators have imposed an anomalous Bohm conductivity inside the discharge channel [8] in an effort to account for fluctuation-enhanced conductivity. Others have added a simple term for the contribution of electron-wall scattering to the mobility [7,9], or have used a combination of both Bohm transport and wall scattering [10]. With the right set of input values for the conductivity, these simulations can accurately reproduce Hall discharge operation, but they provide little insight into the actual physics of the device.

The primary physics problem for the Hall discharge, and for many small-scale magnetized plasmas, is understanding the mechanisms dictating cross-field electron transport. Using the results of an extensive diagnostic effort put forth to measure the plasma properties inside a laboratory xenon Hall discharge [12,13], we presented an analysis giving the effective conductivity inside the Hall discharge with alumina walls [1]. This study showed fluctuation-induced transport to be a promising mechanism, but ignored electron-wall interactions as a source of enhanced conductivity. We and others have elucidated the behavior of plasma instabilities in the Hall discharge plasma [14–18], but have not yet completed a full theoretical description of fluctuation-induced transport.

The current study aims to predict the rates of electron-wall collisions in the Hall discharge and to determine if electron-wall interactions are important to cross-field transport. We begin by assuming a Maxwellian EEDF and using our experimental results to determine the rate of electron and ion wall loss in the discharge channel. We then extend our analysis to using a simplified Boltzmann equation to calculate the EEDF. The Boltzmann equation couples the EEDF to the collisional processes in the plasma, including the electron-wall interactions, and to the electric and magnetic fields. We use the Boltzmann model to compare and discuss anomalous conductivity and mechanisms of EEDF formation.

## II. EXPERIMENTS

### A. Background

In our experimental study of mobility in a Hall discharge, we used a simple version of Ohm’s law to calculate the collision frequency needed for the electrons to cross the magnetic field,

$$J_{ez} = \frac{\nu_{\text{eff}}^2}{\nu_{\text{eff}}^2 + \omega_{ce}^2} \left( \frac{n_e e^2}{m \nu_{\text{eff}}} \right) E_z. \quad (1)$$

Here,  $e$  and  $m$  are the charge and mass of the electron, respectively. This quadratic equation can be solved for the effective collision frequency  $\nu_{\text{eff}}$  if the electron current density  $J_{ez}$ , axial electric field  $E_z$ , electron density  $n_e$ , and cyclotron frequency  $\omega_{ce}$  are known from experiments. If the xe-

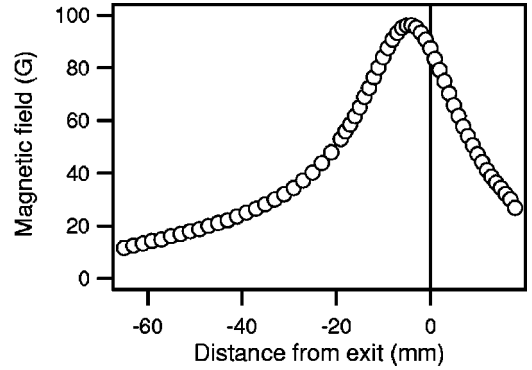


FIG. 2. Magnetic field profile in the Hall discharge channel. The exit of the discharge is at  $Z=0$ , whereas the anode is located at  $Z \approx -70$  mm.

non neutral density  $N$  and electron temperature  $k_B T_e$  are also known and a Maxwellian distribution is assumed for the electrons, the result  $\nu_{\text{eff}}$  can be compared to the electron-neutral momentum-transfer collision frequency  $\hat{\nu}_M$ , which should be the dominant collision frequency for the low-density, weakly ionized plasma present in the Hall discharge channel.

This comparison was made for the Hall parameter  $\omega_{ce} \tau$  in the previous paper, where  $\tau = 1/\nu_{\text{eff}}$ . Several time-average plasma properties were measured at different positions in the channel. The radial magnetic field was measured with a Hall-effect sensor with the plasma off. The magnetic field profile is shown in Fig. 2 for reference. The plasma potential was measured using a hot-filament emissive probe, allowing the calculation of  $E_z$  and an estimate of the electron temperature  $k_B T_e$ . The axial ion velocity  $V_i$  was measured using laser-induced fluorescence velocimetry. These measurements are described in more detail in [12,13]. The electron density was measured with a combination of cylindrical and planar Langmuir probes [19]. With  $n_e$  and  $V_i$  known, the electron current density could be calculated from the total discharge current  $I$ ,

$$J_{ez} = I/A_{\text{chan}} - en_e V_i, \quad (2)$$

where  $A_{\text{chan}}$  is the cross-sectional area of the discharge channel, allowing Eq. (1) to be solved for  $\nu_{\text{eff}}$  (or  $\omega_{ce} \tau$ ). In all, we have direct experimental measurements of  $B$ ,  $n_e$ ,  $V_i$ , the plasma potential  $\phi_p$ , and the floating potential  $\phi_f$  at each point in the channel, leading to values for  $E_z$ ,  $J_{ez}$ ,  $\nu_{\text{eff}}$ , and the electron temperature  $k_B T_e$ . These plasma properties are the basis for all the analysis described in this paper. The properties are plotted in [1] and will not be redisplayed here.

Figure 3 shows a comparison of  $\nu_{\text{eff}}$  and  $\hat{\nu}_M$  for a portion of the discharge channel. Here, we have assumed a constant value of  $N = 10^{19} \text{ m}^{-3}$  for the neutral density. To calculate  $\hat{\nu}_M$ , we used a Maxwellian distribution about the experimental electron temperature  $k_B T_e$  and a cross section for momentum transfer in xenon obtained from the SIGLO database [20]. Throughout this paper, quantities calculated assuming a Maxwellian EEDF will be denoted by the caret (e.g.,  $\hat{Q}$ ). Clearly, electron-neutral collisions are not sufficient to account for electron transport in the Hall discharge.

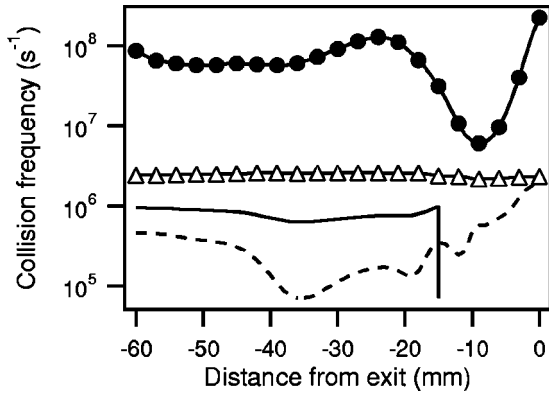


FIG. 3. Effective collision frequency for electron transport  $\nu_{\text{eff}}$  ( $\bullet$ ), compared to  $\hat{\nu}_M$  ( $\Delta$ ),  $\tilde{\nu}_{\text{wall loss}}$  from Eq. (3) (---), and  $\hat{\nu}_{\text{wall loss}}$  from Eq. (6) (—).

### B. Electron-wall interaction for a Maxwellian

Some further comparison can be made to  $\nu_{\text{eff}}$  using only the experimental data and assuming a Maxwellian distribution for the electrons. The rate at which electrons striking the wall are lost to recombination can be calculated from a continuity equation for the ions,

$$\begin{aligned} \frac{d(n_e V_i)}{dz} &= n_e \hat{\nu}_1 - n_e \tilde{\nu}_{\text{wall loss}} \\ &\rightarrow \tilde{\nu}_{\text{wall loss}} \\ &= \hat{\nu}_1 - \frac{1}{n_e} \frac{d(n_e V_i)}{dz}. \end{aligned} \quad (3)$$

Here,  $\hat{\nu}_1$  is the ionization collision frequency, calculated using a cross section from the SIGLO database [20]. We have assumed a quasineutral plasma ( $n_e \approx n_i$ ). The wall-loss rate must be the same for the electrons and the ions to maintain the no-current condition at the insulator wall.

We can make another estimate of the wall-loss rate  $\tilde{\nu}_{\text{wall loss}}$  without using data for  $n_e$  and  $V_i$ . For an arbitrary isotropic distribution, the flux of electrons to a planar surface in the presence of a repelling sheath of potential  $\phi$  is given as [21]

$$\Gamma = n_e \int_{c^*}^{\infty} \frac{1}{4} c f(c) \left[ 1 - \left( \frac{c^*}{c} \right)^2 \right] dc, \quad (4)$$

where  $f$  is the distribution function in speed ( $c$ ) space and  $c^* = \sqrt{2e\phi/m}$ . Integrating over a Maxwellian about  $k_B T_e$  gives the familiar result

$$\Gamma = n_e \frac{\bar{c}}{4} \exp\left(\frac{-e\phi}{k_B T_e}\right). \quad (5)$$

Here,  $\bar{c}$  is the mean (thermal) speed of the electrons. The characteristic transit frequency of electrons across the channel of width  $w$  will be  $\bar{c}/w$ , so we can approximate the rate at which electrons are lost to the wall as

$$\hat{\nu}_{\text{wall loss}} = \frac{\bar{c}}{w} (1 - \hat{\gamma}_{\text{eff}}) \exp\left(\frac{-e\phi_{\text{wall}}}{k_B T_e}\right). \quad (6)$$

The effective coefficient of secondary electron emission  $\hat{\gamma}_{\text{eff}}$  is the number of secondary electrons produced when one electron strikes the insulator wall, averaged over a Maxwellian electron energy distribution,

$$\hat{\gamma}_{\text{eff}} = \frac{\int_{-\infty}^{\infty} \int_{-\infty}^{\infty} \int_0^{\infty} \gamma(\epsilon) c_{\perp} f_{\text{Max}}(\mathbf{c}) d\mathbf{c}}{\int_{-\infty}^{\infty} \int_{-\infty}^{\infty} \int_0^{\infty} c_{\perp} f_{\text{Max}}(\mathbf{c}) d\mathbf{c}}. \quad (7)$$

where  $c_{\perp}$  is the velocity normal to the wall, corresponding to the innermost integral. The secondary emission coefficient is generally given as a function of electron energy by

$$\gamma(\epsilon) = (\epsilon/\epsilon_1)^p, \quad (8)$$

where  $\epsilon_1$  is the first-crossover energy, defined by  $\gamma(\epsilon_1) = 1$ . Assuming  $p = 1$ ,  $\hat{\gamma}_{\text{eff}}$  for a Maxwellian is given by  $\hat{\gamma}_{\text{eff}} = 2k_B T_e / \epsilon_1$ . We use  $\epsilon_1 = 25$  eV for alumina ( $\text{Al}_2\text{O}_3$ ), from experimental measurements by Dawson [22]. The scarcity and uncertainty of the data for  $\gamma(\epsilon)$  at energies below  $\epsilon_1$  makes the choice of  $p$  somewhat arbitrary. The choice of  $p = 1$  will be justified in a later section. Ion-induced secondary electron generation is small for low-energy xenon ions and is neglected [23].

The wall-sheath potential  $\phi_{\text{wall}}$  is found by balancing the net flux of electrons to the wall to that of the ions, assuming that the ions enter the sheath at the Bohm velocity. The situation is complicated when  $\hat{\gamma}_{\text{eff}}$  approaches a critical value near unity; at this point, the sheath reaches the charge saturation limit, and  $\hat{\gamma}_{\text{eff}} \approx 1$ . This phenomenon is described in detail in [24]. The resultant expression for the potential is

$$\begin{aligned} \phi_{\text{wall}} &= \frac{k_B T_e}{e} \ln \left[ (1 - \hat{\gamma}_{\text{eff}}) \sqrt{\frac{M}{2\pi m}} \right], \quad \hat{\gamma}_{\text{eff}} < 0.983, \\ \phi_{\text{wall}} &= 0.88 k_B T_e, \quad \hat{\gamma}_{\text{eff}} \geq 0.983, \end{aligned} \quad (9)$$

where  $M$  is the xenon ion mass.

We can now compare the wall-loss rates of electrons calculated from Eq. (6) to  $\nu_{\text{eff}}$  and  $\hat{\nu}_M$ . The results are given in Fig. 3. Several phenomena are of interest here. For most of the discharge channel, the wall-loss rate estimated for a Maxwellian EEDF is much higher than  $\tilde{\nu}_{\text{wall loss}}$  given by Eq. (3); however, near the exit of the discharge, the wall sheath undergoes charge saturation. The loss rate for a Maxwellian drops to nearly zero ( $\hat{\gamma}_{\text{eff}} \approx 1$ ), whereas the experiments ( $\tilde{\nu}_{\text{wall loss}}$ ) suggest that the loss rate actually increases near the exit. Understanding the reasons for this discrepancy is the key to determining if electron-wall collisions are significant to electron transport in the Hall discharge. In a plasma, an absorbing wall preferentially removes high-energy electrons from the system. The assumption that a Maxwellian distribution is maintained in this plasma may lead to over-

predicting the frequency of electron-wall collisions, leading to charge saturation. We turn to a model for the EEDF to examine this possibility.

### III. BOLTZMANN EQUATION

#### A. Background

The idea of solving the Boltzmann equation to study near-wall conductivity was recently explored by Degond *et al.* [25]. For the case of no gas-phase collisions, Degond *et al.* solve the electron Boltzmann equation using a Hilbert expansion method and compare the results to a Monte Carlo simulation. Both models produce a “double-hump” EEDF, with the energy of the second hump increasing towards the anode. Later versions of these models, expanded to include elastic and inelastic gas-phase collisions, produced different results [26]. The two-population distribution remained, but the height of the high-energy peak was significantly diminished, presumably due to increased thermalization. The phenomenological model for the electron-wall interaction used in these studies describes several classes of scattered electrons and will be explained further in a later section.

#### B. Approximations

The steady state Boltzmann equation for the electrons can be written as

$$\mathbf{c}\nabla_{\mathbf{x}}f - \frac{e}{m}(\mathbf{E} + \mathbf{c}\times\mathbf{B})\nabla_{\mathbf{c}}f = \left(\frac{\delta f}{\delta t}\right)_{\text{coll}}, \quad (10)$$

where  $f$  is the electron velocity distribution function (EVDF),  $\mathbf{c}$  is the vector electron velocity,  $\nabla_{\mathbf{x}}$  is the gradient operator with respect to positional space, and  $\nabla_{\mathbf{c}}$  is the gradient in velocity space. We proceed to a solution of this equation following several approximations. In the Lorentz (two-term) approximation, the EVDF  $f$  is separated into a component that is predominantly isotropic  $f_0$  and components that skew the distribution in the directions of the electric field and the  $\mathbf{E}\times\mathbf{B}$  drift:

$$f(\mathbf{c}) = f_0(c) + (\mathbf{c}\cdot\mathbf{E})f_1(c) + [\mathbf{c}\cdot(\mathbf{B}\times\mathbf{E})]f_2(c). \quad (11)$$

The functions  $f_1$  and  $f_2$  are also isotropic, and when weighted by  $cE$  and by  $c(\mathbf{B}\times\mathbf{E})$ , result in small perturbations on the predominantly isotropic core. Therefore, this model may not be appropriate for EVDFs with extreme anisotropy due to high drift energies or beamlike electrons streaming from the cathode neutralizer, e.g., [27]. We will not address the anisotropy of the EVDF in this paper.

The directions of the electric field  $\mathbf{E}$  and magnetic field  $\mathbf{B}$  are taken as purely axial ( $\mathbf{z}$ ) and radial ( $\mathbf{r}$ ), respectively. We neglect spatial gradients in the axial direction by making the local field approximation. The cyclotron radius of the electrons in the Hall discharge is 10–100 times smaller than the shortest electron mean free path, except near the anode. Thus, the EEDF is formed locally, at distances below the mean free path. In other words, due to magnetic confinement, an electron reaches equilibrium with the local fields on time scales shorter than those which control diffusion across

a characteristic length scale of the plasma. The axial variation of the EEDF is determined solely by the axial change in plasma properties. This approach has been successfully applied to the determination of the EEDF in a cylindrical magnetron [28], a discharge similar to the Hall discharge in size, pressure, and magnetic field strength. In this paper, we will present results for points in the discharge channel where the magnetic field is strong, between  $Z=0$  and  $Z=-30$  mm. We also treat the plasma as uniform in the azimuthal direction due to symmetry, and in the radial direction, as electrons can freely diffuse along radial magnetic field lines. For a more detailed explanation of the local and nonlocal approaches to solving the Boltzmann equation, see [29].

After removal of the spatial gradient term, the solution proceeds by substituting the perturbation expression Eq. (11) into Eq. (10) and simplifying the equation to a scalar expression for the isotropic EVDF  $f_0$ . This procedure is detailed for elastic collisions in [30] and for elastic and inelastic collisions in [31]. For this study, we restrict the inelastic collisions to ionization and wall-loss collisions. Excitation collisions are neglected, as they will behave qualitatively similarly to ionization. Electron-electron and electron-ion collisions are also neglected. A simple estimate of the electron-ion collision frequency using the Coulomb logarithm for plasma conditions found inside the Hall discharge channel ( $n_e=10^{18} \text{ m}^{-3}$ ,  $kT_e=10 \text{ eV}$ ) results in a collision frequency of  $2\times 10^5 \text{ s}^{-1}$ , an order of magnitude lower than that for electron-neutral collisions. We also neglect the temperature of the background xenon neutrals ( $\approx 0.1 \text{ eV}$ ). These details may be added to the model in a later study.

We convert from speed to kinetic energy using  $u=kc^2$ , where the constant  $k$  is defined such that  $u$  is expressed in eV. The subscript is also dropped from the isotropic EVDF  $f_0$ , and we have let  $f(c)=f(u)$  for convenience. After adding wall-loss collisions and separating the elastic and inelastic terms, the Boltzmann equation becomes

$$\begin{aligned} \frac{4}{3}\left(\frac{eE}{m}\right)^2 k^2 \frac{d}{du} \left[ \left( \frac{N\sigma_M u^2}{k\omega^2 + N^2\sigma_M^2 u} \right) \frac{df}{du} \right] + N \frac{2m}{M} \frac{d}{du} [u^2\sigma_m f] \\ = uN\sigma_I(u)f(u) - (u+u_1)N\sigma_I(u+u_1)f(u+u_1) \\ + \sqrt{ku}\nu_{\text{wall}}(u)f(u), \end{aligned} \quad (12)$$

where  $\sigma_I$  is the ionization cross section and  $u_1$  is the threshold energy for ionization (12.12 eV for xenon). From left to right, the terms in Eq. (12) represent Joule heating, elastic collisions, loss of electrons due to ionization, return of electrons from ionizing collisions, and loss of electrons to the wall.

Equation (12) assumes that electrons are transported across the magnetic field lines primarily by elastic collisions with xenon atoms. As an alternative, we substitute the experimentally determined collision frequency  $\nu_{\text{eff}}$  for  $N\sigma_M c$  in Eq. (12). The effective collision frequency attempts to include effects left out by this model, such as fluctuation-induced transport, and results in more realistic solutions. With this substitution, Eq. (12) becomes

$$\begin{aligned} & \frac{4}{3} \left( \frac{eE}{m} \right)^2 k^{3/2} \frac{d}{du} \left[ \left( \frac{u^{3/2} \nu_{\text{eff}}}{\omega^2 + \nu_{\text{eff}}^2} \right) \frac{df}{du} \right] + Nk^{1/2} \frac{2m}{M} \frac{d}{du} [u^{3/2} \nu_{\text{eff}} f] \\ & = uN\sigma_1(u)f(u) - (u+u_1)N\sigma_1(u+u_1)f(u+u_1) \\ & \quad + \sqrt{ku} \nu_{\text{wall}}(u)f(u). \end{aligned} \quad (13)$$

The two momentum-transfer models represented in Eqs. (12) and (13) will be compared later in the paper. Unless otherwise noted, all the results displayed in this paper were calculated using the experimentally determined collision frequency described in Sec. II,  $\nu_{\text{eff}}$ .

### C. Electrons produced by ionization

In Eq. (13), ionization and wall loss are treated as inelastic excitation collisions that do not produce electrons. We can improve this by introducing secondary electron terms to the model, following [32]. We start by deriving the contribution of electrons produced by ionization. The expressions derived here will be modified to describe secondary electrons from the wall later in the paper. We define  $q$  as the cross section for producing secondary or scattered electrons of particular energies. The collision term for ionization is then expressed as

$$\begin{aligned} \left( \frac{\delta f(u)}{\delta t} \right)_{\text{ion}} &= \frac{cN}{u} \int_{2u+u_1}^{\infty} u' q_{\text{sec}}^1(u', u) f(u') du' \\ & \quad + \frac{cN}{u} \int_{u+u_1}^{2u+u_1} u' q_{\text{sca}}^1(u', u) f(u') du' \\ & \quad - cN\sigma_1(u)f(u). \end{aligned} \quad (14)$$

The first two terms on the right-hand side are the source terms for secondary and scattered electrons, respectively. The third term is the ionization loss term. The integrals involving  $q$  can be simplified using  $\delta$ -function expressions:

$$\begin{aligned} q_{\text{sec}}^1(u', u) &= \sigma_1(u') \delta(u - \tilde{u}), \\ q_{\text{sca}}^1(u', u) &= \sigma_1(u') \delta[u - (u' - u_1 - \tilde{u})]. \end{aligned} \quad (15)$$

Here,  $\delta$  is the Dirac delta function and  $\tilde{u}$  is the energy of the secondary electron. We use the value  $\tilde{u} = (u' - u_1)/2$ , representing a case in which the energy remaining from the inelastic collision is divided equally between the secondary and scattered electrons. Plugging Eq. (15) into Eq. (14), we arrive at

$$\begin{aligned} \left( \frac{\delta f(u)}{\delta t} \right)_{\text{ion}} &= \frac{2cN}{u} (2u+u_1) \sigma_1(2u+u_1) \\ & \quad \times f(2u+u_1) - cN\sigma_1(u)f(u). \end{aligned} \quad (16)$$

### D. Electron-wall interaction

To complete Eq. (13), we must describe the details of the electron-wall interaction and add the secondary electrons from the wall. By analogy to Eqs. (4) and (6), we write

$$\nu_{\text{wall}}(u) = \frac{1}{w} \sqrt{\frac{u}{k}} \left( 1 - \frac{u^*}{u} \right) H(u - u^*), \quad (17)$$

where  $u^* = e\phi_{\text{wall}}$  and the Heaviside step function  $H$  enforces  $\nu_{\text{wall}}(u) = 0$  for  $u < u^*$ . This expression takes into account the fact that only electrons with enough radial velocity to penetrate the wall sheath will strike the wall. Electrons that cannot penetrate the sheath scatter elastically and specularly and do not impact the EEDF or contribute to cross-field transport.

An electron that does strike the wall suffers one of three fates. This electron will either scatter elastically (but not necessarily specularly), recombine with an ion, or generate a secondary electron. Following Degond *et al.* [25], we will express these three fates in the secondary electron emission coefficient  $\gamma$ . The total frequency at which electrons are returned from the wall is expressed as

$$\nu_{\text{ret}}(u) = \gamma_t(u - u^*) \nu_{\text{wall}}(u), \quad (18)$$

where  $\gamma(\epsilon) = \gamma_t(\epsilon)$  is determined as in Eq. (8). We evaluate  $\gamma_t$  at the energy of the electron after it has decelerated in the sheath. Note that Eq. (7) does not take this into account. In Eq. (7), the expression for  $\gamma(\epsilon)$  and the limits of the integral should reflect the slowing of the electron in the sheath:

$$\hat{\gamma}_{\text{eff}} = \frac{\left( \int_{-\infty}^{\infty} \int_{-\infty}^{\infty} \int_{c^*}^{\infty} \gamma(u - u^*) c_{\perp} f_{\text{Max}}(\mathbf{c}) d\mathbf{c} \right)}{\left( \int_{-\infty}^{\infty} \int_{-\infty}^{\infty} \int_{c^*}^{\infty} c_{\perp} f_{\text{Max}}(\mathbf{c}) d\mathbf{c} \right)}. \quad (19)$$

We use  $p = 1$  to avoid this complication. It turns out that for  $p = 1$ , both Eqs. (7) and (19) give  $\hat{\gamma}_{\text{eff}} = 2k_B T_e / \epsilon_1$ . The results of the Boltzmann solver are not very sensitive to  $p$  for  $0.5 \leq p \leq 1$ .

Electrons returned from the wall occur in two groups: elastically scattered electrons and ‘‘true secondaries’’ from the lattice. We treat the first-crossover energy  $\epsilon_1$  as a threshold for generating true secondaries. This allows us to write  $\gamma_e$  and  $\gamma_s$ , the secondary emission coefficients for elastically scattered and true secondary electrons, respectively, as

$$\begin{aligned} \gamma_e &= \gamma_t \quad (u - u^* \leq \epsilon_1), \\ \gamma_e &= 2 - \gamma_t \quad (\epsilon_1 < u - u^* \leq \epsilon_2), \\ \gamma_e &= 0 \quad (\text{otherwise}), \end{aligned} \quad (20)$$

and

$$\gamma_s = \gamma_t - \gamma_e, \quad (21)$$

where  $\epsilon_2$  is defined as  $\gamma(\epsilon_2) = 2$ . These expressions are phenomenological and quite arbitrary, but they will prove useful in demonstrating how the form of  $\gamma$  impacts the EEDF. The secondary coefficients are shown in Fig. 4. In [25], the form used for  $\gamma_t$  as asymptotically approaches 2, removing the need for the third case in Eq. (20). To complete the specification of the electron-wall interaction, we assume that true secondary

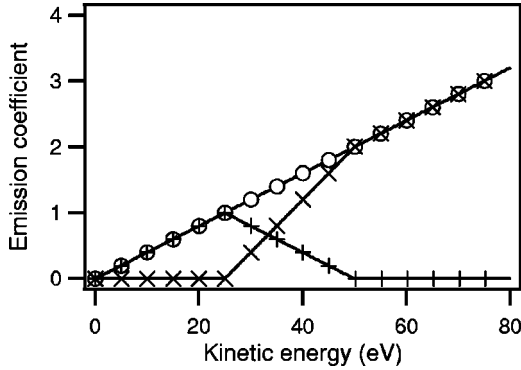


FIG. 4. Secondary emission coefficients used for this study, from Eq. (8) with  $p=1$  and Eqs. (20) and (21):  $\gamma_t$  ( $\circ$ ),  $\gamma_e$  ( $+$ ),  $\gamma_s$  ( $\times$ ).

electrons emitted from the wall are cold: they reenter the EEDF with the wall-sheath potential energy  $u^*$ . So, expressing the wall collisions in the same form as ionizing collisions, we reach

$$\left(\frac{\delta f(u)}{\delta t}\right)_{\text{loss}} = [1 - \gamma_e(u - u^*)] \nu_{\text{wall}}(u) f(u) \quad (22)$$

and

$$\begin{aligned} \left(\frac{\delta f(u)}{\delta t}\right)_{\text{sec}} &= \frac{1}{\sqrt{u}} \delta(u - u^*) \\ &\times \int_{u^*}^{\infty} \sqrt{u'} \gamma_s(u' - u^*) \nu_{\text{wall}}(u') f(u') du'. \end{aligned} \quad (23)$$

Since the elastically scattered electrons lose no energy, they essentially reduce the wall loss. Substituting Eqs. (16), (17), (22), and (23) into Eq. (13), we arrive at

$$\begin{aligned} \frac{d}{du} \left[ \mathcal{D}(u) \frac{df}{du} \right] + \frac{d}{du} [\mathcal{G}(u)f] - \mathcal{J}(u)f(u) - \mathcal{W}(u)f(u) \\ = -\mathcal{I}(u) - \mathcal{S}(u). \end{aligned} \quad (24)$$

For convenience, we have expressed the equation in terms of collision operators [28]:

$$\mathcal{D}(u) = \frac{4}{3} \left( \frac{eE}{m} \right)^2 k^{3/2} u^{3/2} \left( \frac{\nu_{\text{eff}}}{\nu_{\text{eff}}^2 + \omega^2} \right),$$

$$\mathcal{G}(u) = \frac{2m}{M} k^{1/2} u^{3/2} \nu_{\text{eff}},$$

$$\mathcal{J}(u) = uN\sigma_I(u),$$

$$\mathcal{I}(u) = 2(2u + u_1)N\sigma_I(2u + u_1)f(2u + u_1),$$

$$\mathcal{W}(u) = [1 - \gamma_e(u - u^*)] \frac{u}{w} \left( 1 - \frac{u^*}{u} \right) H(u - u^*),$$

and

$$\mathcal{S}(u) = \delta(u - u^*) \int_{u^*}^{\infty} \gamma_s(u' - u^*) \frac{u'}{w} \left( 1 - \frac{u^*}{u'} \right) f(u') du'.$$

The equation must satisfy one boundary condition at infinity,

$$f \rightarrow 0 \quad \text{as} \quad u \rightarrow \infty, \quad (25)$$

and the normalization condition

$$\int_0^{\infty} F du = \int_0^{\infty} \sqrt{u} f du = 1. \quad (26)$$

### E. Wall-sheath potential

In order to solve this system, we need a way to calculate the wall-sheath potential. Rather than using Eq. (9), a formula based on the no-current condition at the wall, we use a local electron balance analogous to Eq. (3). Electron production by ionization is balanced by the net outflow of electron current and by recombination at the wall:

$$\begin{aligned} \int_0^{\infty} uN\sigma_I(u)f(u)du &= \frac{\sqrt{k}}{en_e} \frac{dJ_e}{dz} + \int_{u^*}^{\infty} [1 - \gamma_t(u - u^*)] \\ &\times \frac{u}{w} \left( 1 - \frac{u^*}{u} \right) f(u) du. \end{aligned} \quad (27)$$

The wall potential  $u^*$  is chosen on the grid to approximately satisfy this balance. This avoids making the assumption of the Bohm criterion for the ions for a non-Maxwellian plasma; however, we can use Eq. (9) as a reality check on the results of the calculation.

### F. Numerical solution

This Boltzmann equation system can be solved iteratively in order to self-consistently determine the wall potential from the calculated EEDF and the experimental input data. At each location  $Z$  in the discharge channel, the local values of  $B$ ,  $E$ ,  $n_e$ , and  $V_i$  from [1], along with  $\nu_{\text{eff}}$  from Eq. (1) and the value  $N = 10^{19} \text{ m}^{-3}$ , are input into Eq. (24). Following [28], the system of equations (24)–(26) is solved using second-order finite differences on a constant- $\Delta u$  grid. The boundary condition at  $\infty$  is expressed in the last linear equation of the system. The normalization condition, Eq. (26), is expressed as the first equation using Simpson's rule, resulting in a matrix that is tridiagonal except for the first row. Each cycle generates a solution for the distribution function  $f$  and the wall potential  $\phi_{\text{wall}}$ . The electron-return term from ionization  $\mathcal{I}$ , which involves off-grid evaluations, is calculated based on the previous solution using cubic-spline interpolation. Similarly, the integral for wall secondary electrons  $\mathcal{S}$  is calculated based on the previous solution. A relative change  $|1 - f_{i+1}/f_i| < 10^{-5}$  occurs at all points in fewer than 50 iterations.

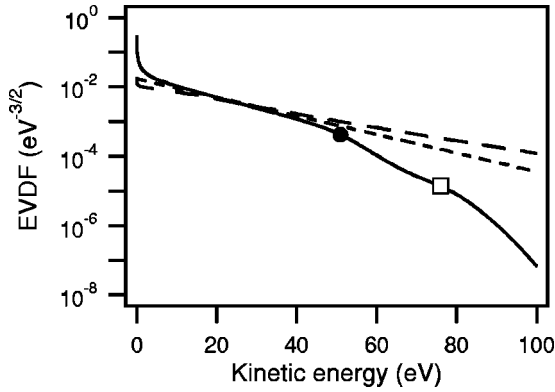


FIG. 5. Calculated EVDF  $f$  at  $Z = -6$  mm for 200-V operation (—), compared to Maxwellian at experimental  $T_e$  (---) and  $f$  for  $\nu_{\text{wall}}(u) = 0$  (-·-·). Points  $u = u^*$  (●) and  $u = u^* + \epsilon_1$  (□) are also indicated for the calculated  $f$ .

#### IV. RESULTS

##### A. General results

Figure 5 shows the EVDF  $f$  calculated using the experimental  $\nu_{\text{eff}}$  in the ionization/acceleration zone of the discharge ( $Z = -6$  mm) for a 200-V operation. On this type of plot, a Maxwellian EVDF is a straight line. The calculated  $f$  agrees well with a Maxwellian at the experimentally estimated electron temperature at low energy, but begins to deviate at high energy. Electrons above the wall-sheath potential  $u^*$  are quickly lost to the wall, causing the distribution to drop rapidly. The wavy shape of the distribution above  $u^*$  is due solely to the expressions used for  $\gamma_i$  and  $\gamma_e$ : The tail of the EEDF mimics the shape of the  $\gamma_e$  curve in Fig. 4. True secondary electrons start to appear at  $u = u^* + \epsilon_1$ , and  $\gamma_e$  decreases according to Eqs. (20) and (21). A distribution function calculated assuming no wall collisions [ $\nu_{\text{wall}}(u) = 0$ ] is also shown. The average energy of this distribution is significantly higher than the experimental electron temperature. Wall-loss collisions are needed to correctly express the energy balance for the electrons.

The apparent large population of very low energy (0–2 eV) electrons is unrealistic—the solution should remain Maxwellian, since elastic collisions dominate in this region. This appears to be a numerical artifact due to the normalization expression. As described in Sec. III F, the normalization condition is written as one of the system of linear equations to be solved. Normalization is achieved as the EEDF is solved, rather than being enforced at the end of integration. This precludes the use of an unphysical second boundary condition and makes the iteration very stable when compared to marching solution methods. The disadvantage of this technique is that as  $u \rightarrow 0$ , the solution  $f$  is artificially “pulled up” to achieve normalization. This occurs well below the ionization threshold  $u_1$  and the wall-potential energy  $u^*$ , and so does not significantly affect the results of this study. The net effect is to lower the average energy of the distribution, which results in a slight underestimation (5–10%) of the various collision frequencies calculated from the EEDF.

Figure 6 compares the EVDF  $f$  from Fig. 5 to that calculated assuming no secondary electrons are emitted from the

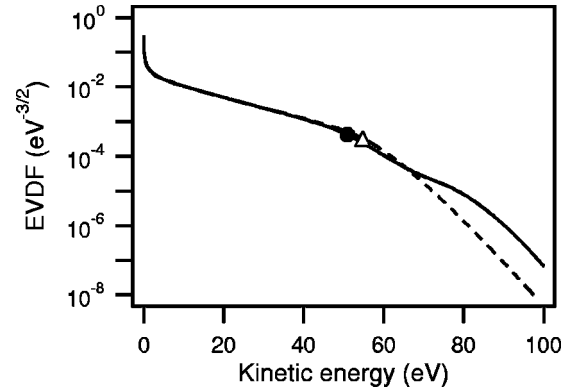


FIG. 6. Calculated EVDF  $f$  (—) and point  $f(u^*)$  (●) compared to  $f$  (---) and  $f(u^*)$  ( $\Delta$ ) calculated with  $\gamma_i = 0$ , for 200-V operation at  $Z = -6$  mm.

walls ( $\gamma_i = 0$ ). Qualitatively, the two distributions are quite similar; however, the truncation of the tail beyond  $u = u^*$  occurs at slightly higher energy when no secondaries are created. This is because the balance equation used to solve for  $u^*$ , Eq. (27), changes little with  $f$ . The ionization rate is very sensitive to the value of  $f$  near the ionization threshold, but not to  $f$  at high energies. So, the total wall loss is essentially fixed by the experimental (constant) current flux  $dJ_e/dz$ . Setting  $\gamma_i = 0$  simply causes the wall potential to increase to match the correct wall-loss rate. The average energy of the distribution is not significantly changed. The tail of the distribution also loses its wavy shape.

We can compare the results of our calculations to experiment by finding the effective electron temperature of the distribution,

$$k_B T_{\text{eff}} = \frac{2}{3} \bar{u} = \frac{2}{3} \int_0^\infty u F du. \quad (28)$$

Recall that the EEDF  $F = \sqrt{u} f$ . This comparison is shown in Fig. 7. The temperatures agree quite well in the part of the channel where local electron kinetics are expected to hold. The fact that the experimental electron temperature is reproduced within a few eV suggests that we have correctly formulated the energy gain and loss terms in the Boltzmann equation. It also suggests that using  $\nu_{\text{eff}}$  for momentum trans-

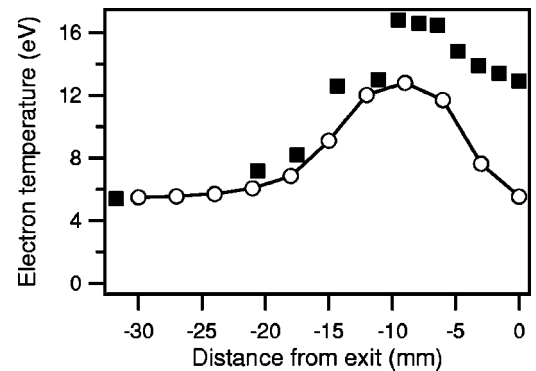


FIG. 7. Electron temperature  $k_B T_{\text{eff}}$  (○) from Eq. (28) compared to  $k_B T_e$  from experiment (■), for 200-V operation.

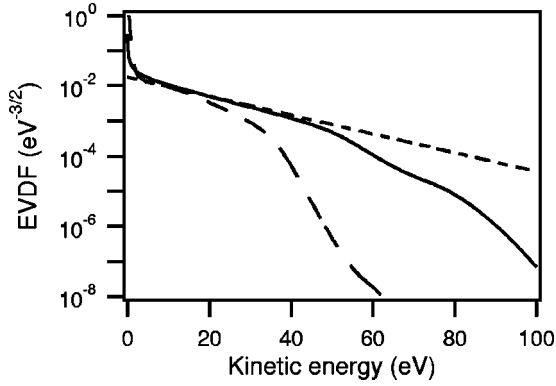


FIG. 8. EVDF  $f$  calculated with  $\nu_M = \nu_{\text{eff}}$  (—) compared to  $f$  calculated with  $\nu_M = Nc\sigma_M$  (---) and Maxwellian at  $k_B T_e$  (-.-), for 200-V operation at  $Z = -6$  mm.

fer in the simulation was an appropriate approximation. This is borne out in Fig. 8. Here, we compare the EVDF in the ionization zone ( $Z = -6$  mm) calculated using  $\nu_M = \nu_{\text{eff}}$  to that using  $\nu_M = Nc\sigma_M$  for momentum transfer, e.g., Eq. (12). Using only electron-neutral collisions, the heating term in the Boltzmann equation is too small to allow  $f$  to reach the appropriate electron temperature.

### B. Collision frequencies

In order to compare different electron-transport mechanisms in the plasma, we use the calculated  $f$  at each point in the channel to calculate the frequencies at which various collisions occur:

$$\bar{\nu}_M = \frac{1}{\sqrt{k}} \int_0^\infty u f(u) N \sigma_M(u) du, \quad (29)$$

$$\bar{\nu}_I = \frac{1}{\sqrt{k}} \int_{u_I}^\infty u f(u) N \sigma_I(u) du, \quad (30)$$

$$\bar{\nu}_{\text{wall}} = \frac{1}{\sqrt{k}} \int_{u^*W}^\infty u \left(1 - \frac{u^*}{u}\right) f(u) du. \quad (31)$$

The overbar (e.g.,  $\bar{Q}$ ) is used to denote a quantity averaged over the calculated EEDF, as opposed to that averaged over a Maxwellian distribution. Here,  $\bar{\nu}_{\text{wall}}$  represents the total frequency of electron-wall collisions, regardless of the electron's fate.

These three collision frequencies are compared to  $\nu_{\text{eff}}$  in Fig. 9. For most of the channel, electron-neutral momentum-transfer collisions dominate ionization and wall collisions; however, near the channel exit, electron-wall collisions become as important as gas-phase collisions. The experimental collision frequency  $\nu_{\text{eff}}$  is much higher than the others throughout the channel. At the closest,  $\bar{\nu}_{\text{wall}}$  is nearly an order of magnitude lower than  $\nu_{\text{eff}}$ . This suggests that some mechanism other than wall scattering is responsible for the high cross-field transport in the Hall discharge channel.

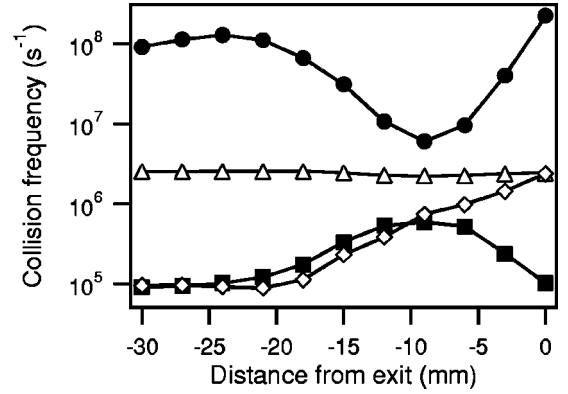


FIG. 9. Comparison of collision frequencies  $\nu_{\text{eff}}$  (●),  $\bar{\nu}_M$  (△),  $\bar{\nu}_I$  (■), and  $\bar{\nu}_{\text{wall}}$  (◇) inside the discharge channel for 200-V operation, as calculated from Eqs. (29)–(31). Note that while this figure has the same scale as Fig. 3 on the left axis, the bottom axis is different.

The frequency of electron-neutral momentum-transfer collisions is essentially constant throughout the channel because we have assumed a constant value for the neutral density  $N$ . In reality,  $N$  should decrease near the exit due to ionization. Elastic collisions are less sensitive to electron temperature than ionization collisions because there is no threshold, so  $\bar{\nu}_M$  is determined almost solely by  $N$ . Unfortunately,  $N$  is one of the most difficult parameters to measure inside the Hall discharge channel. The value of  $N = 10^{19} \text{ m}^{-3}$  is an approximate upper bound based on the mass flow injected into the channel and the sound speed of xenon at 1000 K. For  $\bar{\nu}_M$  to approach  $\nu_{\text{eff}}$ ,  $N$  would have to be significantly higher. The impact of experimental uncertainty in the EEDF calculations will be explored later in the paper.

### C. Wall-sheath potential

The EEDF solver outputs  $\phi_{\text{wall}}$  as well as  $f$ , so we can compare the wall potentials predicted with this model to those given by Eq. (9). We will use the effective electron temperature  $k_B T_{\text{eff}}$ , defined in Eq. (28), for comparison. The

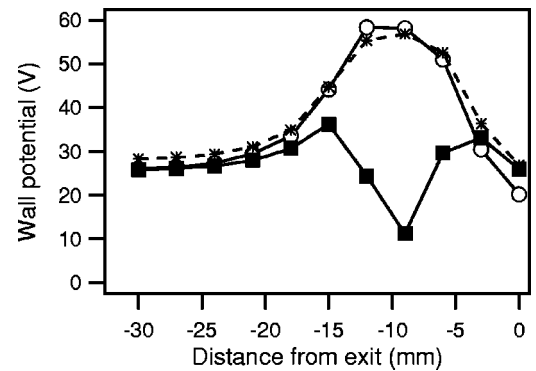


FIG. 10. Wall potential calculated from  $f$  and Eq. (27) (○) compared to results of Eq. (9) with  $\hat{\gamma}_{\text{eff}} = 2k_B T_{\text{eff}} / \epsilon_1$  (■) and to Eq. (9) with imposed  $\bar{\gamma}$  (\*), for 200-V operation.

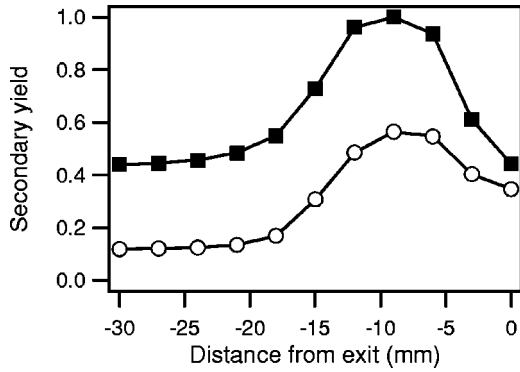


FIG. 11. Comparison of  $\bar{\gamma}$  (○) from the Boltzmann model to  $\hat{\gamma}_{\text{eff}}$  (■) for a Maxwellian.

results are given in Fig. 10. The potentials agree quite well in the cooler part of the channel; however, from  $Z = -15$  mm to  $Z = -6$  mm, Eq. (9) predicts that the wall is approaching charge saturation, whereas the Boltzmann solver predicts a high wall potential. The reason for this is that the Boltzmann solver produces a lower number of reflected and secondary electrons. We can define an average emission coefficient for the calculated EEDF as  $\bar{\gamma} = \bar{\nu}_{\text{ret}} / \bar{\nu}_{\text{wall}}$ , using the definitions in Eqs. (18) and (31). The average secondary coefficient for the calculated  $f$  is compared to that of a Maxwellian in Fig. 11. If we use  $\bar{\gamma}$  in place of  $\hat{\gamma}_{\text{eff}}$  in Eq. (9) and then solve for  $\phi_{\text{wall}}$ , the results agree quite well (Fig. 10). This suggests that assigning the Bohm velocity at  $k_B T_{\text{eff}}$  to ions entering the wall sheath is acceptable for calculating the sheath potential, as long as  $\bar{\gamma}$  can be accurately determined.

The reason for the discrepancies in the wall potential is simply that the Boltzmann solver predicts wall collision rates much lower than those for a Maxwellian EEDF. In the Boltzmann solver, high-energy electrons are preferentially removed from the distribution. In the steady state, there are not enough collisions to maintain a high temperature in the tail of the distribution. Assuming a Maxwellian at one temperature produces a much higher flux of electrons to the wall. At the low wall potentials encountered in the charge-saturation limit, it is unrealistic to maintain an energetic tail in the distribution, at least with the form we have chosen for  $\gamma$ . The

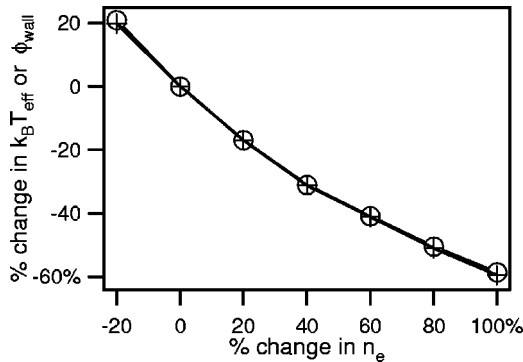


FIG. 12. Variation in electron temperature  $k_B T_{\text{eff}}$  (○) and wall potential  $\phi_{\text{wall}}$  (■) with electron density at  $Z=0$  mm.

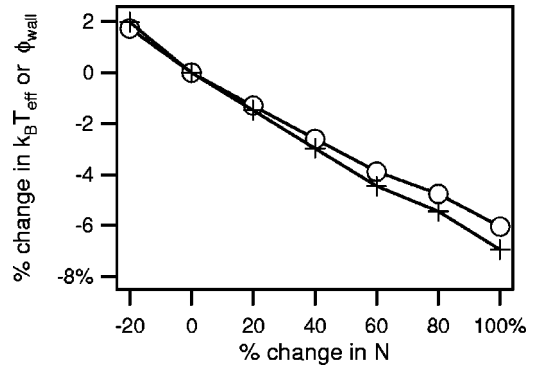


FIG. 13. Variation in electron temperature  $k_B T_{\text{eff}}$  (○) and wall potential  $\phi_{\text{wall}}$  (■) with neutral density at  $Z=0$  mm.

choices we have made result in an EEDF that agrees well with the experimental electron temperature.

### V. SENSITIVITY ANALYSIS

Since the Boltzmann solver depends strongly on experimental data for inputs, it is prudent to examine the sensitivity of the analysis to experimental uncertainty. We focus on the two plasma parameters that are most difficult to measure, the electron density  $n_e$  and the neutral density  $N$ . The other main inputs to the code, the ion velocity and total discharge current, can be measured with very high accuracy. Error in the electron density  $n_e$  has a significant impact on the results because the input parameter  $\nu_{\text{eff}}$  depends on  $n_e$  through Eqs. (1) and (2). Increasing  $n_e$  decreases  $\nu_{\text{eff}}$ , resulting in a lower electron temperature and a lower wall potential, as shown in Fig. 12.

The dependence on  $N$  is different, in that changing  $N$  does not impact  $\nu_{\text{eff}}$ . Instead, increasing  $N$  increases energy losses to ionization, decreasing the electron temperature. The overall ionization rate increases, so the wall potential drops to allow more wall losses. These two effects are shown in Fig. 13. The key result of the sensitivity analysis is that the main conclusions of this paper remain valid even if the errors in  $N$  and  $n_e$  are significant. As shown in Fig. 14, the important wall collision frequencies decrease with  $n_e$ , so that wall collisions are never significant to electron transport. In the case

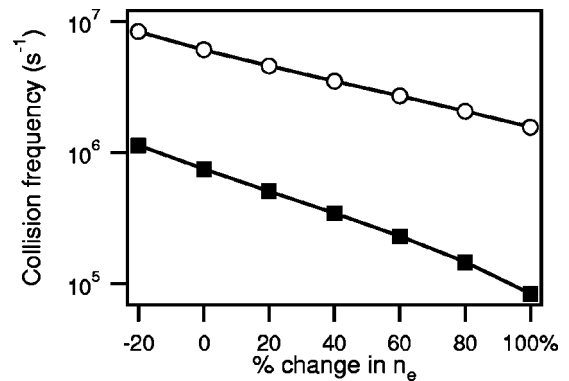


FIG. 14. Variations in  $\nu_{\text{eff}}$  (○) and  $\bar{\nu}_{\text{wall}}$  (■) with electron density at  $Z = -9$  mm, the location where  $\bar{\nu}_{\text{wall}}$  is closest to  $\nu_{\text{eff}}$ .

of  $N$ , the only collision frequency that changes rapidly with  $N$  is  $\bar{\nu}_M$ ; however,  $N$  would have to be unrealistically increased by a factor of 10 or more in order for  $\bar{\nu}_M$  to be comparable to  $\nu_{\text{eff}}$ .

## VI. CONCLUSION

A combination of experimental and analytical efforts have been used to study electron-wall collisions inside the discharge channel of a laboratory Hall discharge. Experimental results indicate that the rate at which electrons are lost to the wall is much lower than that predicted for a Maxwellian EEDF at the experimental electron temperature. The simple Boltzmann equation model developed to examine this discrepancy appears to explain some of the important physics. Since the channel wall preferentially absorbs fast electrons, the EEDF cannot maintain a hot tail. This reduces the steady state rate of electron-wall collisions, which in turn reduces the number of secondary electrons emitted from the wall. The wall sheath does not appear to reach the charge-saturation limit, so the rate of electron-wall collisions never approaches a level comparable to  $\nu_{\text{eff}}$ , the collision frequency needed to explain cross-field transport. Large uncertainties in the electron and neutral number densities do not

change the general conclusions. For now, we maintain the same conclusion found in [1]: fluctuation-induced electron transport is the best candidate to explain the anomalous mobility in the Hall discharge plasma.

However, the behavior of the plasma-wall system in the Hall discharge does depend on a delicate balance of factors. In particular, the specific form and magnitude chosen for the secondary emission coefficient  $\gamma$  can strongly influence the results. More work remains to better understand the exact behavior of a low-energy electron striking a rough ceramic surface in the presence of a repelling sheath. Furthermore, a strong theoretical understanding of fluctuation-induced transport in small-scale plasmas needs to be developed to make the concept useful to scientists and engineers designing the next generation of magnetized plasma sources.

## ACKNOWLEDGMENTS

This work was sponsored by the Air Force Office of Scientific Research. The authors would like to thank P. Degond, N. Gascon, M. Dudeck, S. Barral, A. A. Ivanov, M. Bacal, and G. Karabadzhak for helpful discussions on electron kinetics and electron-wall interactions.

- 
- [1] N.B. Meezan, W.A. Hargus, Jr., and M.A. Cappelli, *Phys. Rev. E* **63**, 026410 (2001).
  - [2] G.S. Janes and R.S. Lowder, *Phys. Fluids* **9**, 1115 (1966).
  - [3] A.I. Morozov and A.P. Shubin, *Pisma Zh. Tekh. Fiz.* **10**, 28 (1984) [*Sov. Tech. Phys. Lett.* **10**, 12 (1984)].
  - [4] A.I. Morozov and A.P. Shubin, *Fiz. Plazmy* **10**, 1262 (1984) [*Sov. J. Plasma Phys.* **10**, 728 (1984)].
  - [5] A.I. Morozov and A.P. Shubin, *Fiz. Plazmy* **10**, 1271 (1984) [*Sov. J. Plasma Phys.* **10**, 734 (1984)].
  - [6] J. Fife and M. Martinez-Sanchez, AIAA Paper No. 97-3052, 33rd AIAA Joint Propulsion Conference, Seattle, WA, 1997 (unpublished).
  - [7] J.P. Boeuf and L. Garrigues, *J. Appl. Phys.* **84**, 3541 (1998).
  - [8] E. Fernandez and M.A. Cappelli, *Bull. Am. Phys. Soc.* **45**(7), 166 (2000).
  - [9] L. Garrigues, A. Heron, J.C. Adam, and J.P. Boeuf, *Plasma Sources Sci. Technol.* **9**, 219 (2000).
  - [10] G.J.M. Hagelaar, J. Bareilles, L. Garrigues, and J.P. Boeuf, *J. Appl. Phys.* **91**, 5592 (2002).
  - [11] J. Szabo, M. Martinez-Sanchez, and O. Batischev, AIAA Paper No. 2000-3653, 36th AIAA Joint Propulsion Conference, Huntsville, AL, 2000 (unpublished).
  - [12] W.A. Hargus, Jr. and M.A. Cappelli, *Appl. Phys. B: Lasers Opt.* **B72**, 961 (2001).
  - [13] W.A. Hargus, Jr. and M.A. Cappelli, *J. Propulsion Power* **18**, 159 (2002).
  - [14] E. Chesta *et al.*, *IEEE Trans. Plasma Sci.* **29**, 582 (2001).
  - [15] E. Chesta, N.B. Meezan, and M.A. Cappelli, *J. Appl. Phys.* **89**, 3099 (2001).
  - [16] E.Y. Choueiri, *Phys. Plasmas* **8**, 1411 (2001).
  - [17] G. Guerrini and C. Michaut, *Phys. Plasmas* **6**, 343 (1999).
  - [18] A.A. Litvak and N.J. Fisch, *Phys. Plasmas* **8**, 648 (2001).
  - [19] N. B. Meezan and M. A. Cappelli, AIAA Paper No. 2000-3420, 36th AIAA Joint Propulsion Conference, Huntsville, AL, 2000 (unpublished).
  - [20] CPAT and KINEMA software, [www.siglo-kinema.com](http://www.siglo-kinema.com)
  - [21] F.F. Chen, in *Plasma Diagnostic Techniques*, edited by R.H. Huddlestone and S.L. Leonard (Academic, New York, 1965), p. 157.
  - [22] P.H. Dawson, *J. Appl. Phys.* **37**, 3644 (1966).
  - [23] K.S. Moon, J. Lee, and K. Whang, *J. Appl. Phys.* **86**, 4049 (1999).
  - [24] E. Ahedo, P. Martinez-Cerezo, and M. Martinez-Sanchez, AIAA Paper No. 2001-3323, 37th AIAA Joint Propulsion Conference, Salt Lake City, UT, 2001 (unpublished).
  - [25] P. Degond, V. Latocha, L. Garrigues, and J.P. Boeuf, *Transp. Theory Stat. Phys.* **27**, 203 (1998).
  - [26] V. Latocha, L. Garrigues, P. Degond, and J.P. Boeuf, *Plasma Sources Sci. Technol.* **11**, 104 (2002).
  - [27] V.Yu. Fedotov *et al.*, *Phys. Plasmas* **6**, 4360 (1999).
  - [28] E. Passoth *et al.*, *J. Phys. D* **21**, 2655 (1999).
  - [29] U. Kortshagen, C. Busch, and L.D. Tsendin, *Plasma Sources Sci. Technol.* **5**, 1 (1996).
  - [30] G. W. Sutton and A. Sherman, *Engineering Magnetohydrodynamics* (McGraw-Hill, New York, 1965), pp. 129–38.
  - [31] N.P. Carleton and L.R. Megill, *Phys. Rev.* **126**, 2089 (1962).
  - [32] S. Yoshida, A.V. Phelps, and L.C. Pitchford, *Phys. Rev. A* **27**, 2858 (1983).